The Astrophysical Journal Letters, 994:L52 (8pp), 2025 December 1 https://doi.org/10.3847/2041-8213/ae1cbd

Where did Heavy Binaries Go? Gravitational-wave Populations Using Delaunay Triangulation with Optimized Complexity

Rodrigo Tenorio[1,2], Alexandre Toubiana[1,2], Tristan Bruel[1,2], Davide Gerosa[1,2], and Jonathan R. Gair[3]
[1] Dipartimento di Fisica "G. Occhialini," Università degli Studi di Milano-Bicocca, Piazza della Scienza 3, 20126 Milano, Italy; rodrigo.tenorio@unimib.it
[2] INFN, Sezione di Milano-Bicocca, Piazza della Scienza 3, 20126 Milano, Italy
[3] Max Planck Institute for Gravitational Physics (Albert Einstein Institute), Am Mühlenberg 1, 14476, Potsdam, Germany
Received 2025 September 23; revised 2025 November 6; accepted 2025 November 7; published 2025 November 27

Abstract

We investigate the joint mass–redshift evolution of the binary black hole (BBH) merger rate in the latest Gravitational-Wave Transient Catalog (GWTC-4.0). We present and apply a novel nonparametric framework for modeling multidimensional, correlated distributions based on Delaunay triangulation. Crucially, the complexity of the model—namely, the number, positions, and weights of triangulation nodes—is inferred directly from the data, resulting in a highly efficient approach that requires about 1 to 2 orders of magnitude fewer parameters and significantly less calibration than current state-of-the-art methods. We find no evidence for a peak at $M_{\rm tot} \sim 70\,M_\odot$ at low redshifts ($z \sim 0.2$), where it would correspond to the $m_1 \sim 35\,M_\odot$ feature reported in redshift-independent mass spectrum analyses, and we infer an increased merger rate at high redshifts ($z \sim 1$) around those masses, compatible with such a peak. When related to the time-delay distribution from progenitor formation to a BBH merger, our results suggest that sources contributing to the $m_1 \sim 35\,M_\odot$ feature follow a steeper (shallower) time-delay distribution at high (low) redshifts. This hints at contributions from different formation channels—for example, dense environments and isolated binary evolution, respectively—although firm identification of specific formation pathways will require further observations and analyses.

Unified Astronomy Thesaurus concepts: Gravitational wave astronomy (675); Gravitational waves (678); Gravitational wave sources (677)

1. Introduction

The increasing number of binary black holes (BBHs) observed by gravitational-wave (GW) interferometers (B. P. Abbott et al. 2019; R. Abbott et al. 2021a, 2023a, 2024; LIGO Scientific Collaboration et al. 2025c) deepens our understanding of their population in the Universe (LIGO Scientific Collaboration et al. 2025b), eventually revealing their origin out of the multiple proposed formation channels (M. Mapelli 2021; I. Mandel & A. Farmer 2022). A crucial step in this direction is the identification of correlations between parameters and the presence of distinct subpopulations (e.g., T. A. Callister 2024 and references therein).

A key question is whether, and how, the BBH population evolves with redshift and, crucially, whether this evolution depends on the BBH properties. BBHs are the end products of stellar evolution; therefore, their population should depend on the star formation history and properties of galaxies such as metallicity (M. Mapelli et al. 2019; C. J. Neijssel et al. 2019; F. S. Broekgaarden et al. 2021; L. A. C. van Son et al. 2022; L. M. de et al. 2024). Moreover, BBHs involving remnants of previous mergers, formed through dynamical encounters, also contribute to the evolution of the population's properties (D. Gerosa & M. Fishbach 2021; S. Torniamenti et al. 2024; C. S. Ye & M. Fishbach 2024). Finally, the redshift evolution encodes the relative contribution of the different BBH formation channels throughout cosmic history (M. Zevin et al. 2021; M. Mapelli et al. 2022; M. A. Sedda et al. 2023).

Evidence for an evolution of the effective spin distribution with redshift (S. Biscoveanu et al. 2022) was found on the third Gravitational-Wave Transient Catalog (GWTC-3) by LIGO, Virgo, and KAGRA and was further strengthened in their fourth catalog (GWTC-4.0; LIGO Scientific Collaboration et al. 2025b). In contrast, several analyses of GWTC-3 found no evidence for or against a redshift evolution in the mass distribution (A. Ray et al. 2023; V. Gennari et al. 2025; J. Heinzel et al. 2025b; M. Lalleman et al. 2025; J. Sadiq et al. 2025), and first analyses on GWTC-4.0 find similar conclusions (LIGO Scientific Collaboration et al. 2025b).[4]

In this work, we investigate the joint mass–redshift evolution of the BBH merger rate using a novel nonparametric multidimensional approach. In particular, we reconstruct the joint mass–redshift BBH merger rate using Delaunay triangulation (B. Delaunay 1934) and barycentric interpolation. Both the number and locations of the triangulation vertices, as well as their associated weights, are inferred directly from the data through transdimensional Bayesian inference (A. Toubiana et al. 2023). The use of a data-driven interpolation scheme assumes no specific functional (in)dependence between mass and redshift; this allows us to probe a broader parameter space compared to models with closed-form correlations.

Using GWTC-4.0 data,[5] we report a distinct difference in the distribution of masses at $z = 0.2$ and $z = 1.0$ at $M_{\rm tot} \sim 70\,M_\odot$, with no evidence for the presence of a peak in

[4] While S. Rinaldi et al. (2024) did report evidence for such an evolution, their treatment of selection effects is not accurate (R. Essick & M. Fishbach 2024; A. Toubiana et al. 2025).
[5] We analyze the 153 BBH events considered by LIGO Scientific Collaboration et al. (2025b); see their Section 6. Note this includes only those events with less than 1% posterior support for component masses below $3\,M_\odot$.

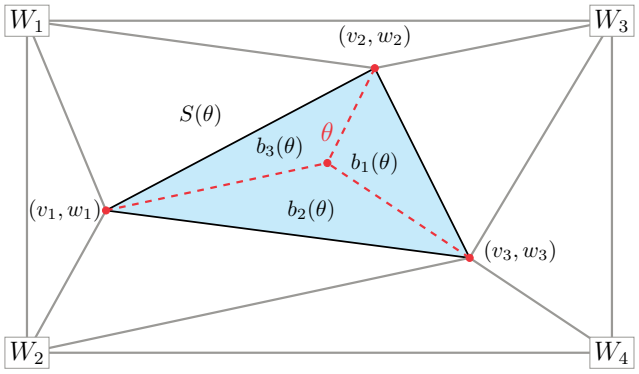

Figure 1. Delaunay triangulation to model the differential merger rate $\log_{10} d_\theta N$ across two variables (on the horizontal and vertical axes). The central red dot represents a location θ where the rate needs to be computed. The highlighted area $S(\theta)$ represents the triangle (simplex in higher dimensions) containing θ whose vertices v_i and weights w_i are inferred from the data. The position of the four corners is fixed in advance, and their weights W_i are inferred from the data. The rate $\log_{10} d_\theta N$ is computed by interpolating the weights at the vertices of $S(\theta)$ using the barycentric coordinates $b_i(\theta)$ associated to θ.

the merger rate at said masses for $z = 0.2$. We then discuss the astrophysical implications of our findings.

2. Mass–Redshift Correlation

We denote the targeted set of source parameters by θ, consisting of total mass $M_{\rm tot}$, mass ratio $q \leqslant 1$, redshift z, spin $\chi_{1,2}$ and cosine of the spin tilts $\cos\vartheta_{1,2}$. To capture potential dependencies between $M_{\rm tot}$ and z, we model the differential number of events $d_\theta N(\theta|\Lambda)$ as

$$\begin{aligned}\log d_\theta N(\theta|\Lambda) = \Delta(M_{\rm tot}, z|\Lambda_\Delta) &+ \log\left[p(q|M_{\rm tot}, \Lambda_q)\right] \\ &+ \log\left[p(\chi_1|\Lambda_\chi)p(\chi_2|\Lambda_\chi)\right] \\ &+ \log\left[p(\cos\vartheta_1, \cos\vartheta_2|\Lambda_\vartheta)\right], \end{aligned} \tag{1}$$

where $\Delta(M_{\rm tot}, z|\Lambda_\Delta)$ represents the (natural log) differential rate as computed by barycentric interpolation using Delaunay triangulation. The hyperparameters Λ_Δ are the number of triangulation vertices, their locations, and the value of the differential rate at those vertices. Figure 1 gives a schematic description of our model; further details are provided in Appendix A. We model the mass-ratio distribution as a broken power law, which is compatible with the marginalized q distribution found in LIGO Scientific Collaboration et al. (2025b; see Appendix B for details). For the spin magnitudes and tilt angles we assume the same functional forms as in the default model by LIGO Scientific Collaboration et al. (2025b). The hyperparameters $\Lambda = (\Lambda_\Delta, \Lambda_q, \Lambda_\chi, \Lambda_\vartheta)$ are inferred through hierarchical Bayesian inference (see Appendix C for details). The differential volumetric rate of GW events is then given by

$$d_\theta \mathcal{R} = \left(\frac{T_{\rm obs}}{1+z}\frac{dV_c}{dz}\right)^{-1} d_\theta N\,, \tag{2}$$

where $T_{\rm obs}$ is the observation time. For completeness, we denote as $m_{1,2}$ the primary and secondary masses.

We limit the domain of inference for the $(M_{\rm tot}, z)$ distribution to $[6, 350]\,M_\odot \times [0, 2.5]$. Priors on triangulation vertices are uniform within this domain, and weights are uniformly distributed along $(-20, 15)$. The number of triangulation nodes is allowed to vary between 4 and 100. Inference is conducted using reversible-jump Markov Chain Monte Carlo as implemented in `eryn` (N. Karnesis et al. 2023). We have verified our findings to be robust against the choice of prior (tests are reported in Appendices B and C).

The left panel of Figure 2 shows the posterior distribution of the volumetric differential rate at two representative redshift values ($z = 0.2$ and $z = 1.0$). Their behavior is different:

1. At $z = 0.2$, the merger rate shows a distinctive peak at $M_{\rm tot} \sim 20\,M_\odot$ and decays in a featureless, power-law-like manner.
2. For $z = 1$, the merger rate increases with respect to that at low redshifts for $M_{\rm tot} \sim 70\,M_\odot$ and appears to have an excess of systems at those masses.

The right panel of Figure 2 shows the credibility for the $z \sim 1$, $M_{\rm tot} \sim 70\,M_\odot$ feature, which we quantify as the posterior probability of $d_\theta\mathcal{R}(M_{\rm tot}, z = 1) > d_\theta\mathcal{R}(M_{\rm tot}, z = 0.2)$. This value is $\gtrsim$95% for $M_{\rm tot} \sim 70\,M_\odot$ and reaches a maximum of 98% at $M_{\rm tot} \sim 63\,M_\odot$. Said increase with redshift is compatible with that found by LIGO Scientific Collaboration et al. (2025c), where the merger rate is modeled as a function of redshift (but not mass) with an ansatz $d_\theta\mathcal{R} \propto (1+z)^\kappa$ and returned $\kappa \sim 3$.

While we cannot definitively claim that the mass distribution at $z = 1.0$ exhibits a peak at $\sim$70 $M_\odot$ owing to the error bars, a corresponding feature at $m_1 \sim 35\,M_\odot$ has been consistently identified since GWTC-2 (R. Abbott et al. 2021b). Our findings suggest that this feature is associated with high-redshift BBHs and disappears by $z = 0.2$. In Appendix D, we show the results of applying our method to (m_1, z) and illustrate how our discussion of the $70\,M_\odot$ feature similarly applies to the $35\,M_\odot$ peak in m_1. Altogether, these results indicate that this high-mass feature in the BBH mass distribution (R. Abbott et al. 2021b, 2023b; LIGO Scientific Collaboration et al. 2025b) varies with redshift. These results are also compatible with S. Rinaldi et al. (2025), who reported tentative evidence for a steeper redshift evolution associated to the $m_1 \sim 35\,M_\odot$ peak than that observed for the power-law component in the GWTC-3 catalog. Future analyses should consider targeting such behavior with more strongly modeled approaches.

Figure 3 presents the outcome of our inference across the $(M_{\rm tot}, z)$ parameter space. The region of high uncertainty roughly aligns with the detection horizon beyond which no BBH mergers were detected; conversely, low uncertainties align with data-dominated regions. We find that BBHs with different masses merge more prominently at different redshifts and that the high-mass prominence appears around $z \sim 0.7$. However, given current uncertainties, no definitive statement about distinct BBH subpopulations can yet be made.

Our findings are not sufficient to establish whether the mass distribution changes with redshift, as the relative difference in rates is consistent with a mass-independent rescaling (see the right panel of Figure 2). The key result of this Letter is the disappearance of the high-mass peak at low redshift.

We characterize the high-redshift appearance of the $\sim$70 $M_\odot$ feature by computing Kullback–Leibler divergence ($D_{\rm KL}$; S. Kullback & R. A. Leibler 1951) between the posterior and the prior on the rate induced by our prior on Λ_Δ For reference, $D_{\rm KL} \lesssim 0.1$ nat between two independent prior draws. As show in the upper-left panel of Figure 2, we find significantly larger values $D_{\rm KL} \sim 2.5$ nat around $M_{\rm tot} \sim 70\,M_\odot$,

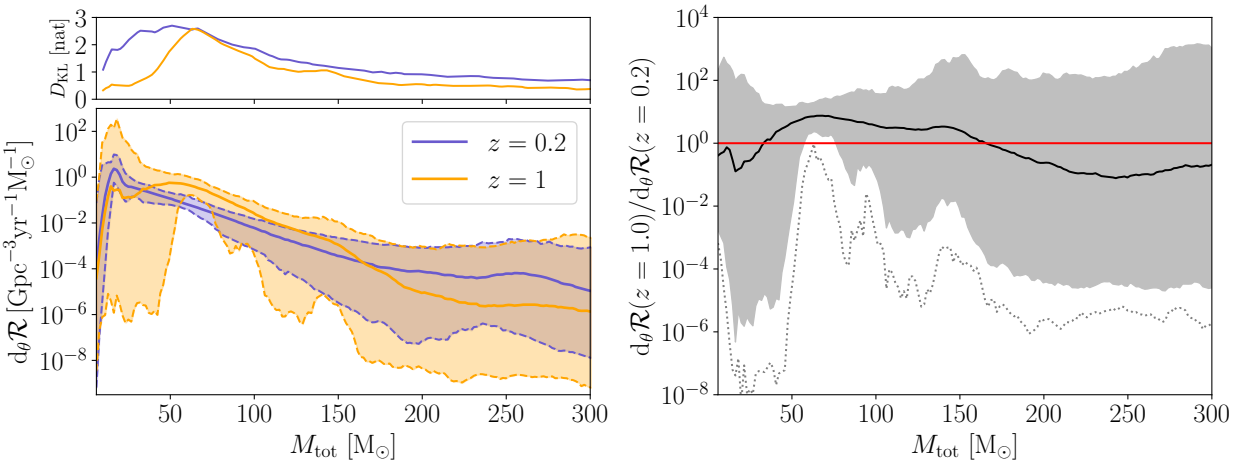

Figure 2. Left: posterior distribution of the volumetric differential rate reconstructed using Delaunay triangulation for two representative redshift values, $z = 0.2$ (purple) and $z = 1$ (orange). Solid curves indicate the medians, while shaded regions encompass 90% symmetric credible intervals. The upper panel shows the $D_{\rm KL}$ between the posterior and prior volumetric differential rate distributions. Right: posterior distribution of the ratio of the volumetric differential rate at the same two representative redshift values. The black solid curve denotes the posterior median. The shaded region contains the symmetric 90% credible interval. The horizontal red line corresponds to $d_\theta\mathcal{R}(z = 0.2) = d_\theta\mathcal{R}(z = 1)$. The dotted line corresponds to the 1.5% credibility interval. The observed difference in rates is thus inconsistent with no evolution of the rate with z at ∼98% credibility but remains consistent with a mass-uniform evolution (the envelope is consistent with a straight line).

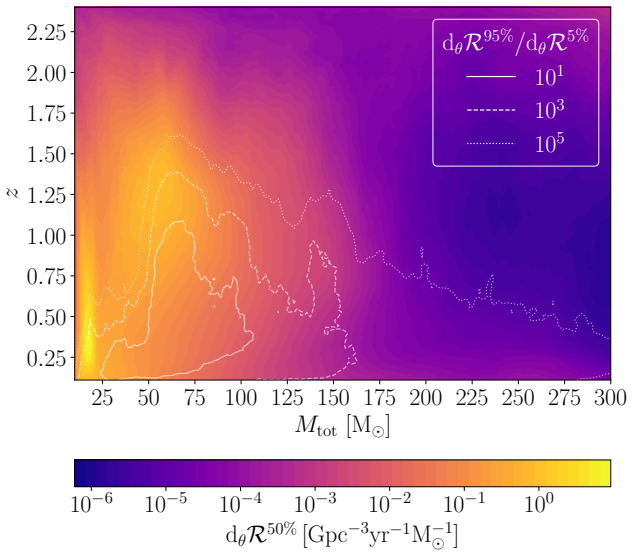

Figure 3. The color scale shows the median (50% quantile) posterior volumetric rate inferred using Delaunay triangulation on GWTC-4.0. The white contours indicate the relative uncertainty on the rate itself, defined as the ratio between the 95% quantile and the 5% quantile.

showing that these results are primarily driven by the observed data. High $D_{\rm KL}$ values align with low relative uncertainties in Figure 3 ($d_\theta\mathcal{R}^{95\%}/d_\theta\mathcal{R}^{5\%} \lesssim 10$), where the inference is dominated by the observed events.

Our results differ from those by LIGO Scientific Collaboration et al. (2025b), which reported no evidence for a mass-dependent redshift evolution of the merger rate using both copulas (C. Adamcewicz & E. Thrane 2022) and binned Gaussian processes (A. Ray et al. 2023). Copulas are suited to identify linear correlations but not the kind of multimodal structures inferred in Figure 3. In the binned Gaussian-process approach, the high-mass feature appears less pronounced at lower redshift, consistent with our findings, though large error bars blur the trend. Their results were shown as probability density functions of m_1 across redshift bins, which are normalized by the total number of events, a very uncertain quantity. As a result, error bars end up broadening. This issue is avoided when working with the volumetric merger rate. The counterpart limitation is that the nonoverlap of confidence bands of the volumetric differential rate at different redshifts is not, by itself, sufficient to establish redshift evolution of the mass distribution. This is shown in the right panel of Figure 2, where a straight line remains consistent with the 90% credibility interval of the rate ratio, which is thus compatible with an overall, rigid rescaling of the $d_\theta\mathcal{R}$. Finally, unlike the binned method, our interpolation points are data driven rather than fixed, potentially capturing finer features by construction.

We also infer a peak in the merger rate at $M_{\rm tot} \sim 20\,M_\odot$ for $z = 0.2$, but the lack of detections at higher redshifts prevents us from confirming or disproving its existence for $z \gtrsim 0.2$. At the high-mass end, the bump at $z = 0.2$ around $M_{\rm tot} \sim 250\,M_\odot$ is likely driven by a single event, GW231123 (A. G. Abac et al. 2025), while the apparent increase in the rate for $M_{\rm tot} \sim 150\,M_\odot$ at $z = 1$ aligns with the inferred source properties of GW190521 (R. Abbott et al. 2020). We caution against overinterpreting such features, which indeed correspond to low values of $D_{\rm KL} \sim 1$ nat.

Our inference on the mass-ratio distribution is consistent with a larger density at $q \gtrsim 0.6$, similarly to what was reported by LIGO Scientific Collaboration et al. (2025b). Details are reported in Appendix B.

The triangulation scheme that best fits the ($M_{\rm tot}$, z) portion of the population has 17^{+25}_{-11} nodes, corresponding to 56^{+75}_{-33} free parameters (90% credible interval). This is 1 to 2 orders of magnitude fewer than those needed by J. Heinzel et al. (2025b) and requires less tuning compared to A. Ray et al. (2023), which computes the final number of bins by rerunning the analysis using increasingly finer grids. Crucially, both of those approaches rely on a fixed two-dimensional grid and are therefore expected to scale poorly with the number of dimensions, whereas Delaunay triangulation is naturally applicable to higher-dimensional correlations. The method proposed by E. Payne & E. Thrane (2023) and N. Guttman et al. (2025) requires a comparable

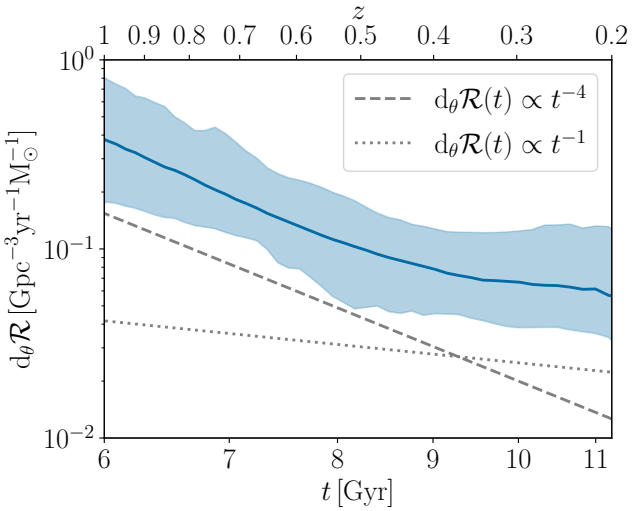

Figure 4. Evolution of the volumetric differential merger rate as a function of cosmic time t in log–log scale evaluated at $M_{\rm tot} = 63\,M_\odot$, i.e., a nominal location where evolution with redshift is tightly constrained. The solid curve indicates the median, while the shaded region encloses the 90% symmetric credible interval. The dashed (dotted) line corresponds to a merger rate evolving as a power law with index –1 (–4) and an arbitrary normalization for reference.

number of parameters but returns the maximum likelihood histogram of data without an associated error. The approach of J. Sadiq et al. (2022), while having a very small number of free parameters, seems to suffer from edge effects where data are scarce or absent; our method correctly returns the prior in these regions of parameter space.

3. Astrophysical Interpretation

Our triangulation-based reconstruction suggests that the known feature in the BBH mass spectrum at $M_{\rm tot} \sim 70\,M_\odot$ ($m_1 \sim 35\,M_\odot$) is primarily due to mergers at $z \gtrsim 0.7$ and fades by $z \sim 0.2$. More specifically, as shown in Figure 4, the evolution of $d_\theta\mathcal{R}$ as a function of cosmic time t between $z = 1$ and $z = 0.2$ appears to follow two regimes, with $d_\theta\mathcal{R}(t) \propto t^{-1}$ at low redshift and a much steeper evolution closer to $d_\theta\mathcal{R}(t) \propto t^{-4}$ at higher redshift. We stress these are indicative trends and not rigorous fits, which would require more data.

Population-synthesis models make predictions for the dependence of the merger rate on the delay time $t_{\rm delay}$, i.e., the time between progenitor formation and BBH merger. In the, likely simplistic, assumption where all stellar progenitors of merging BBHs form in a burst at cosmic time t_0, the merger rate traces the delay-time distribution, $d_\theta\mathcal{R}(t) \sim dN/dt_{\rm delay}$ with $t_{\rm delay} = t - t_0$. The results in Figure 4 are thus informative about the astrophysical channels that generate the $M_{\rm tot} \sim 70\,M_\odot$ feature.

At low redshift, $d_\theta\mathcal{R}(t) \propto t^{-1}$ is compatible with typical predictions for isolated binary evolution, including sources ejected from stellar clusters (see e.g., M. Dominik et al. 2012; K. Belczynski et al. 2016; J. J. Eldridge & E. R. Stanway 2016; A. Lamberts et al. 2016; M. Mapelli et al. 2017).

By contrast, the steeper behavior at higher redshift $d_\theta\mathcal{R}(t) \propto t^{-4}$ is in line with numerical simulations of cluster evolution where BBHs merge inside their host clusters (e.g., C. L. Rodriguez & A. Loeb 2018; M. A. Sedda et al. 2024). Moreover, these dynamically assembled BBHs are, on average, more massive than those from isolated evolution (C. L. Rodriguez et al. 2016; U. N. Di Carlo et al. 2019; F. Antonini & M. Gieles 2020; M. A. Sedda et al. 2024), which would explain their prominence at $M_{\rm tot} \sim 70\,M_\odot$ ($m_1 \sim 35\,M_\odot$; F. Antonini et al. 2023; T. Bruel et al. 2025).

In short, a possible explanation of our findings is that the dense-environment channels, which are predicted to form BBH with higher z and shorter delay, are responsible for the $M_{\rm tot} \sim 70\,M_\odot$ feature, with isolated (and ejected) binaries providing the longer-delay background that dominates at low redshift.

Massive, dense globular clusters match the requirements for this explanation, as they likely tend to form at earlier cosmic times with respect to the global formation of stars in the Universe (N. Choksi et al. 2018; K. El-Badry et al. 2019) and thus naturally give rise to a high-mass contribution to the BBH merger rate that switches off at low redshifts. Numerical analyses of this scenario predict a high-mass BBH peak at $z \gtrsim 2$ that extends to lower redshifts (S. Torniamenti et al. 2024; C. S. Ye & M. Fishbach 2024), suggesting that our observation could in fact correspond to the lower-redshift tail of this peak. Similarly, active galactic nucleus disks are another dense environment favoring hierarchical mergers, which can also produce heavy BBHs with short delays (Y. Yang et al. 2019; H. Tagawa et al. 2020; A. Santini et al. 2023).

Pulsational pair-instability supernovae (PPISNe) have long been invoked to explain the $m_1 \sim 35\,M_\odot$ feature as a pileup of masses at the instability onset (see e.g., S. E. Woosley 2017; C. Talbot & E. Thrane 2018). Recent studies, however, have shown this hypothesis to be in conflict with theoretical predictions of the expected location of the related mass gap or the relative number of systems in this mass range (S. Stevenson et al. 2019; E. Farag et al. 2022; D. D. Hendriks et al. 2023). Moreover, the PPISN channel would require extreme values of nuclear reaction rates, in particular the $^{12}{\rm C}(\alpha, \gamma)^{16}{\rm O}$ reaction rate, to match the black hole (BH) mass distribution inferred from GW observations (see e.g., F. Antonini et al. 2025; H. Tong et al. 2025, for recent analyses). Also, while the interplay between time delays and the dependence of BH maximum mass on progenitor metallicity can give rise to an evolution with redshift of the BH mass spectrum (R. Farmer et al. 2019; S. Mukherjee 2022), this scenario relies preferentially on longer time delays, which are not favored by our analysis. The results presented in this work add to the mounting evidence that this formation channel may not be the preferred one to explain the $m_1 \sim 35\,M_\odot$ feature in the GW spectrum.

Peaks in the BBH mass spectrum at $m_1 \gtrsim 30\,M_\odot$ can also be caused by low-metallicity stars whose structures have not been altered by binary interaction (F. R. N. Schneider et al. 2021, 2023), which then get paired through other processes. The low-metallicity requirement naturally ties this process to redshift through the chemical enrichment of the Universe, but further work is required to assess the compatibility of these models with our results.

We also recover a low-mass peak $M_{\rm tot} \sim 20\,M_\odot$($m_1 \sim 10\,M_\odot$) at $z = 0.2$ (current uncertainties prevent confirmation at $z = 1$). This previously reported feature (R. Abbott et al. 2021b, 2023b; LIGO Scientific Collaboration et al. 2025b) is well explained by isolated binary evolution at near-solar metallicity (P. Agrawal et al. 2023; T. Fragos et al. 2023) or dynamical evolution of stars and compact objects in metal-rich dense clusters (C. S. Ye et al. 2025). More observations are needed to confirm the invariance of this low-mass peak across redshift.

4. Conclusions

We presented a nonparametric reconstruction of the mass–redshift correlation in merging BBH using Delaunay triangulation

and barycentric interpolation. Our analysis of GWTC-4.0 data reveals that the high-mass feature at $M_{\rm tot} \sim 70\,M_\odot$ appears predominantly from $z \gtrsim 0.7$ and is absent at $z = 0.2$. At the same time, we caution against overinterpreting (the medians of) nonparametric reconstructions, which often, including here, come with large statistical errors.

So, where would the heavy binaries have gone? Taken together, our results suggest the presence of a population with $M_{\rm tot} \sim 70 M_\odot$, characterized by a fast-merging component that dominates at high redshift and a slow-merging component that becomes increasingly important at low redshift. While such a trend could arise from multiple formation pathways—such as dense environments for short delays and isolated (and ejected) binaries for long delays—establishing the relative contribution of specific channels requires further observational and theoretical work. This includes investigating potential correlations in other parameters, most notably spins and eccentricity.

Moreover, our findings imply that analyses measuring cosmological parameters from the redshift dependence of the detector-frame mass spectrum (D. F. Chernoff & L. S. Finn 1993; D. Markovic 1993; W. M. Farr et al. 2019; S. Mastrogiovanni et al. 2021; LIGO Scientific Collaboration et al. 2025a) should carefully account for the evolution of the prominence of the high-mass peak with z.

The key strength of using Delaunay triangulation is that the interpolation skeleton, including the number and location of the nodes, is inferred directly from the data. In practice, this optimized complexity reduces the number of parameters by 1 to 2 orders of magnitude compared to the pixelized approach by J. Heinzel et al. (2025b) and attains a good recovery of arbitrary functional forms at a lower tuning cost compared to the binned Gaussian-process approach by A. Ray et al. (2023), both of which rely on a fixed grid. For this reason, we expect our flexible framework to be significantly more efficient at probing correlations in dimensions $\geqslant 3$, making it ideally suited for the forthcoming big-data era of GW astronomy.

Acknowledgments

We thank April Qiu Cheng, Raffi Enficiaud, Jack Heinzel, and Matthew Mould for the discussions. R.T., A.T., T.B., and D.G. are supported by ERC Starting grant No. 945155–GWmining, Cariplo Foundation grant No. 2021-0555, MUR PRIN grant No. 2022-Z9X4XS, Italian–French University (UIF/UFI) grant No. 2025-C3-386, MUR grant "Progetto Dipartimenti di Eccellenza 2023-2027" (BiCoQ), and the ICSC National Research Centre funded by NextGenerationEU. A.T. and D.G. are supported by MUR Young Researchers grant No. SOE2024-0000125. D.G. is supported by MSCA fellowship No. 101149270–ProtoBH. Computational work was performed at CINECA with allocations through INFN and the University of Milano-Bicocca and at NVIDIA with allocations through the Academic Grant program. This research has made use of data or software obtained from the Gravitational Wave Open Science Center.

Software: astropy (T. P. Robitaille et al. 2013), eryn (N. Karnesis et al. 2023), numpy (C. R. Harris et al. 2020), qhull (C. B. Barber et al. 1996), scipy (P. Virtanen et al. 2020).

Appendix A
Delaunay Triangulation for Inference

We seek to represent general multidimensional distributions using an agnostic model with a low computational cost. Our strategy is to construct a transdimensional interpolator for the merger rate using barycentric interpolation on a Delaunay triangulation (B. Delaunay 1934; S. Rippa 1990; V. T. Rajan 1994). The number of triangulation points is allowed to vary through inference, thus modeling arbitrarily simple (or complex) distributions depending on the available information in the data. This method can be applied to parameter spaces of arbitrary dimensionality. While we restrict our application of the method to a two-dimensional parameter space, we describe it in full generality.

We model the differential number of events $d_\theta N(\theta;\Lambda)$ in dimension D. The hyperparameters Λ we aim to infer are the number of triangulation vertices $N_{\rm v}$, their locations v_k, and their weights w_k, where the v_k's live in the same space as θ and the w_k's are real numbers.

In our current implementation, we infer the rate within a D-dimensional box $\mathcal{D}$ so that $d_\theta N(\theta) = 0$ if $\theta \notin \mathcal{D}$. To do so, we place $N_{\rm c} = 2^D$ fixed vertices at the corners of the domain; their associated weights $\{W_k,\, k = 1,\ldots, N_{\rm c}\}$ are allowed to vary. Thus,

$$\Lambda = \{N_{\rm v},\, \{W_k\}_{k=1,\ldots,N_{\rm c}},\, \{v_k,\, w_k\}_{k=1\ldots,N_{\rm v}-N_{\rm c}}\}\,. \tag{A1}$$

The number of free parameters is

$$\begin{aligned} N_{\rm par} &= 1 + N_{\rm c} + (D+1)(N_{\rm v} - N_{\rm c}) \\ &= 1 - D\,2^D + (D+1)N_{\rm v}. \end{aligned} \tag{A2}$$

We denote the (natural log) differential rate as computed by a triangulation with parameters Λ by $\log d_\theta N(\theta|\Lambda) \equiv \Delta(\theta|\Lambda)$. To compute the differential rate at a given point θ, we find the simplex $S(\theta)$ (i.e., triangle if $D = 2$) wherein it lies, compute its barycentric coordinates, and use them to linearly interpolate the weights at their vertices:

$$\Delta(\theta|\Lambda) = \sum_{v\in S(\theta)} w_v b_v(\theta)\,. \tag{A3}$$

We illustrate this process for $D = 2$ in Figure 1. In such case, each triangle $S(\theta)$ has three pairs of vertices and weights $\{(v_1, w_1), (v_2, w_2), (v_3, w_3)\}$ from which one can construct three barycentric coordinates $\{b_1(\theta), b_2(\theta), b_3(\theta)\}$.

The number of expected events within a domain $\mathcal{D}$ for a given triangulation Λ is given by

$$N(\Lambda;\, \mathcal{D}) = \int_{\theta\in\mathcal{D}} {\rm d}\theta\; e^{\Delta(\theta;\Lambda)}\,. \tag{A4}$$

For a single simplex S, Equation (A4) can be expressed in closed form as

$$N(\Lambda;\, S) = D!\,|S| \sum_{i=1}^{D+1} \frac{\exp(w_i)}{\prod_{j\neq i}(w_i - w_j)}\,, \tag{A5}$$

where $|S|$ denotes the generalized volume of S (i.e., the area if $D = 2$) and $w_1, \ldots, w_{D+1}$ are the weights of its vertices.

We construct Delaunay triangulations using `qhull` (C. B. Barber et al. 1996) via `scipy` (P. Virtanen et al. 2020).

Appendix B
Mass-ratio Distribution

The fiducial model by LIGO Scientific Collaboration et al. (2025b) describes the joint $(m_1,\, q)$ distribution as a sum of components, each independent in m_1 and z. This formulation makes the overall distribution nonseparable in m_1 and q, and

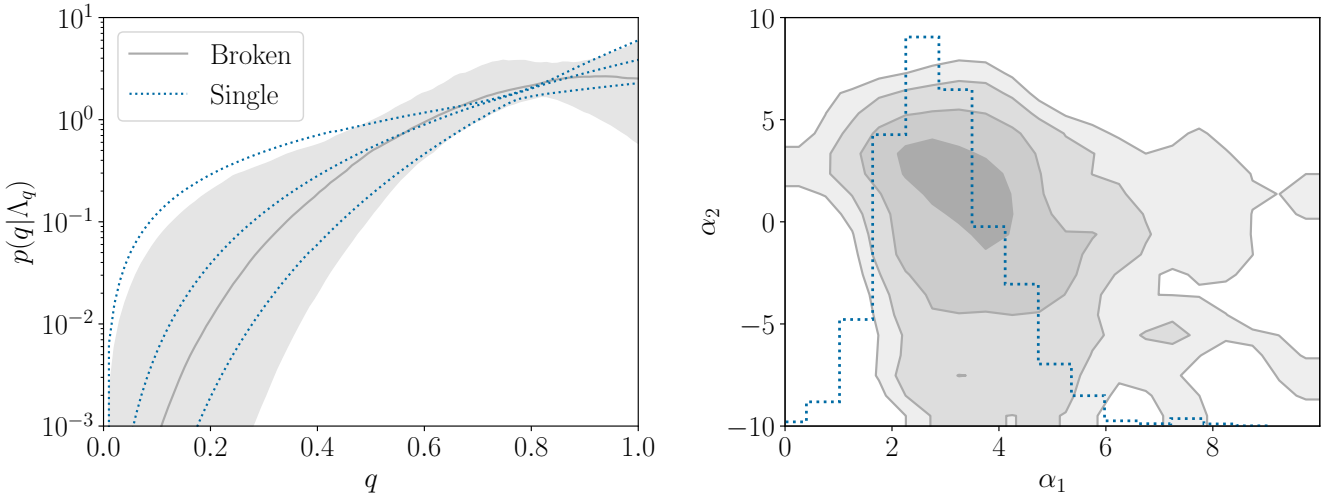

Figure 5. Left: posterior predictive distribution of the mass-ratio distribution. The red (gray) solid line represents the median, while the shaded (dotted) envelope contains the 90% credible interval assuming a broken (single) power-law distribution. Right: posterior distribution of the power-law indices. The gray area represents the posterior probability on (α_1, α_2) for the broken power-law model, while the dotted histogram represents the posterior probability on α_1 for the single power-law model.

this cannot be straightforwardly implemented in our framework. Guided by LIGO Scientific Collaboration et al.'s (2025b) findings (see their Figure 5), we describe the mass-ratio distribution using a broken power law:

$$p(q|\Lambda_q) \propto \begin{cases} 0 & q < q_{\rm min}\,, \\ (q/q_{\rm cut})^{\alpha_1} & q_{\rm min} < q < q_{\rm cut}\,, \\ (q/q_{\rm cut})^{\alpha_2} & q_{\rm cut} \leqslant q. \end{cases} \tag{B1}$$

Prior distributions for $\Lambda_q = (q_{\rm cut}, \alpha_1, \alpha_2)$ are uniform across (0.5, 1.0), (0, 10), and (−10, 10), respectively. The lower end $q_{\rm min} = 3\,{\rm M}_\odot/m_1$ is chosen so that $m_2 > 3\,M_\odot$. The population predictive distribution of q and the hyperposterior distribution of (α_1, α_2) are shown in Figure 5. We observe an enhanced number of mergers at $0.6 \lesssim q \lesssim 0.8$ compared to the single power-law model.

For completeness, we also show the results for a single power law, corresponding to $q_{\rm cut} \to 1$ and/or $\alpha_2 \to \alpha_1$. The conclusions of our work regarding the behavior of the merger rate across ($M_{\rm tot}$, z) are overall unchanged. The main quantitative difference is that the credibility for an enhanced rate at $\sim 70\,M_\odot$ is lower (∼94% versus ∼98%).

Appendix C
Formalism for Hierarchical Inference

We express the population likelihood for observing $N_{\rm obs}$ events with data $\{d_j\} = \{d_1,\ldots,d_{N_{\rm obs}}\}$ for a set of population hyperparameters Λ as (I. Mandel et al. 2019; S. Vitale et al. 2020)

$$p(\{d_j\}|\Lambda) \propto e^{-N_{\rm det}(\Lambda)} \prod_{j=1}^{N_{\rm obs}} \left\langle \frac{d_\theta N(\theta|\Lambda)}{\pi_{\rm PE}(\theta)} \right\rangle_{\theta\sim p(\theta|d_j)}, \tag{C1}$$

where $p(\theta|d_j)$ and $\pi_{\rm PE}(\theta)$ are the posterior and prior distribution of the parameters describing event j. The number of expected events $N_{\rm det}(\Lambda)$ is given by

$$N_{\rm det}(\Lambda) = \left\langle \frac{d_\theta N(\theta|\Lambda)}{\pi_{\rm inj}(\theta)} p({\rm det}|\theta) \right\rangle_{\theta\sim\pi_{\rm inj}(\theta)}, \tag{C2}$$

where

$$p({\rm det}|\theta) = \int_{d>\,\text{threshold}} p(d|\theta)\, dd \tag{C3}$$

is the probability of detecting a source with parameters θ, $p(d|\theta)$ is the likelihood for data d, and the integral is restricted to realizations d that exceed the detection threshold (defined via the chosen ranking statistic).

For cosmological calculations, we assume the `Planck15` cosmology as implemented in `astropy` (T. P. Robitaille et al. 2013).

Equations (C1) and (C2) are computed via Monte Carlo integration, here indicated with $\langle\cdot\rangle$. Selection effects are estimated using the injection campaign presented by R. Essick et al. (2025). We set the population likelihood to zero for hyperparameters that yield a variance in the Monte Carlo estimators greater than one (C. Talbot & J. Golomb 2023; LIGO Scientific Collaboration et al. 2025b; M. Mancarella & D. Gerosa 2025). We verify the robustness of this choice by rerunning our inference using thresholds of 0.8 and 1.2. The results are qualitatively unchanged; the credibility for an enhanced merger rate at $\sim 70\,M_\odot$ is ∼95% instead of ∼98% for the 1.2 threshold.

As discussed in the main text, the priors on the modeled part of the population parameters (Λ_q, Λ_χ, Λ_ϑ) are taken equal to those of LIGO Scientific Collaboration et al. (2025b), while the prior on the triangulation parameters is uniform across the area of interest for the triangulation vertices and along (−20, 15) for the triangulation weights. The implied prior range on $d_\theta N$ (or equivalently $\mathrm{d}_\theta\mathcal{R}$) is compatible with (if not more conservative than) those used in similar nonparametric approaches (J. Heinzel et al. 2025a, 2025b; S. Alvarez-Lopez et al. 2025). We also verified the robustness of our results against prior choices by extending the weight prior down to (−25, 15), which lowers the induced prior on $d_\theta N$ by 2 to 3

orders of magnitude. The results for $z = 0.2$ remain unchanged. For $z = 1$, the lower end of the posterior distribution on $d_\theta\mathcal{R}$ lowers so that the credibility for $d_\theta\mathcal{R}(z = 1) > d_\theta\mathcal{R}(z = 0.2)$ is slightly lower (∼94% instead of ∼98%). We stress that the key result of this work, namely, the disappearance of the peak at low redshifts, is not affected by prior choices. The lack of an obvious choice for the prior range of w_i suggests nonparametric population models are better suited to conduct inference in the observed space, where the domain of inference is naturally limited to data-dominated regions (A. Toubiana et al. 2025).

We also compute the $D_{\rm KL}$ (S. Kullback & R. A. Leibler 1951) to compare the posterior volumetric merger rate to its prior distribution at any given $(M_{\rm tot}, z)$. The prior distribution on $\log_{10} d_\theta\mathcal{R}(M_{\rm tot}, z)$, denoted by $p(\log_{10} d_\theta\mathcal{R})$ for simplicity, is constructed by sampling the prior distribution of Λ_Δ (i.e., number of vertices, positions, and weights) and computing the corresponding $\log_{10} d_\theta\mathcal{R}(M_{\rm tot}, z)$. The posterior distribution, denoted $p(\log_{10} d_\theta\mathcal{R}|\{d_j\})$, is computed analogously by sampling from $p(\Lambda_\Delta|\{d_j\})$. To approximate these probability densities, we generate 10^4 samples in every $(M_{\rm tot}, z)$ of interest and fit a Gaussian kernel density estimator. The $D_{\rm KL}$ (in nat) for any given $(M_{\rm tot}, z)$ is then computed as

$$D_{\rm KL} = \left\langle \ln \frac{p(\log_{10} d_\theta\mathcal{R}|\{d_j\})}{p(\log_{10} d_\theta\mathcal{R})} \right\rangle_{\log_{10} d_\theta\mathcal{R}\sim p(\log_{10} d_\theta\mathcal{R}|\{d_j\})} . \quad \text{(C4)}$$

Appendix D
Population Inference for (m_1, z)

To facilitate comparison with other studies, Figure 6 shows the results of our method applied to the joint (m_1, z) distribution instead of $(M_{\rm tot}, z)$. The significance of the enhanced rate at $\sim 35\,M_\odot$ at $z = 1$ versus $z = 0.2$ is slightly lower than for $(M_{\rm tot}, z)$ (∼95% versus ∼98%, right panel of Figure 6), likely due to larger measurement uncertainties in m_1, but the qualitative disappearance of the high-mass peak at low redshift persists.

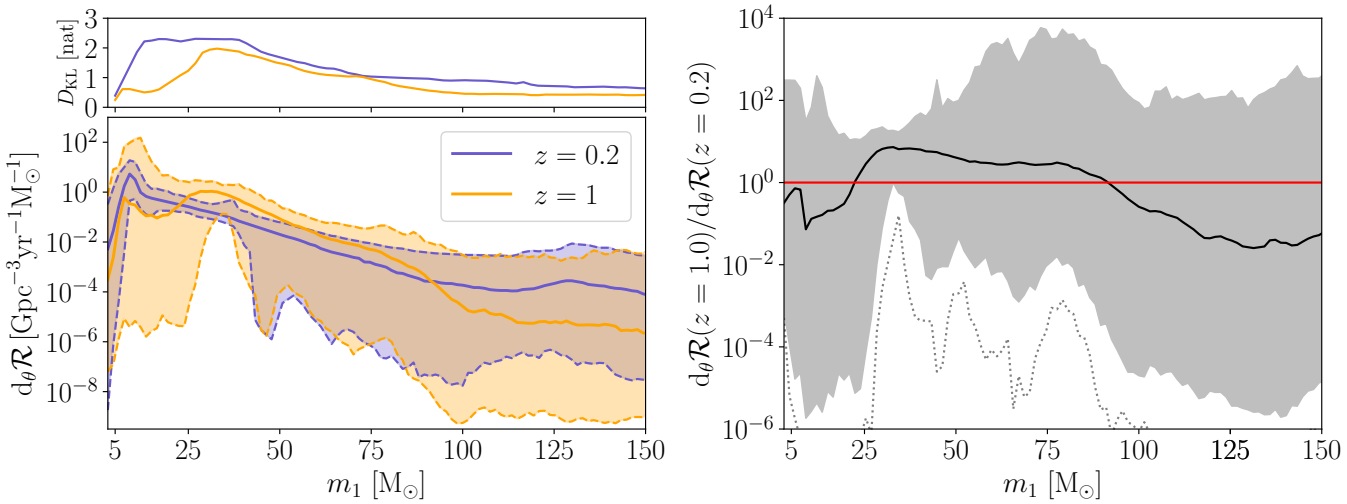

Figure 6. Joint reconstruction of the (m_1, z) BBH volumetric merger rate, mirroring Figure 2 in the main body of the Letter. A constant rate is excluded with 95% credibility (i.e., the solid red line is included in the 90% symmetric credible interval, here shaded in gray).

ORCID iDs

Rodrigo Tenorio https://orcid.org/0000-0002-3582-2587
Alexandre Toubiana https://orcid.org/0000-0002-2685-1538
Tristan Bruel https://orcid.org/0000-0002-1789-7876
Davide Gerosa https://orcid.org/0000-0002-0933-3579
Jonathan R. Gair https://orcid.org/0000-0002-1671-3668

References

Abac, A. G., Abouelfettouh, I., Acernese, F., et al. 2025, ApJL, 993, L25
Abbott, B. P., Abbott, R., Abbott, T. D., et al. 2019, PhRvX, 9, 031040
Abbott, R., Abbott, T. D., Abraham, S., et al. 2020, PhRvL, 125, 101102
Abbott, R., Abbott, T. D., Abraham, S., et al. 2021a, PhRvX, 11, 021053
Abbott, R., Abbott, T. D., Abraham, S., et al. 2021b, ApJ, 913, L7
Abbott, R., Abbott, T. D., Acernese, F., et al. 2023a, PhRvX, 13, 041039
Abbott, R., Abbott, T. D., Acernese, F., et al. 2023b, PhRvX, 13, 011048
Abbott, R., Abbott, T. D., Acernese, F., et al. 2024, PhRvD, 109, 022001
Adamcewicz, C., & Thrane, E. 2022, MNRAS, 517, 3928
Agrawal, P., Hurley, J., Stevenson, S., et al. 2023, MNRAS, 525, 933
Alvarez-Lopez, S., Heinzel, J., Mould, M., & Vitale, S. 2025, arXiv:2506.20731
Antonini, F., & Gieles, M. 2020, PhRvD, 102, 123016
Antonini, F., Gieles, M., Dosopoulou, F., & Chattopadhyay, D. 2023, MNRAS, 522, 466
Antonini, F., Romero-Shaw, I., Callister, T., et al. 2025, arXiv:2509.04637
Barber, C. B., Dobkin, D. P., & Huhdanpaa, H. 1996, ACM Trans. Math. Software, 22, 469
Belczynski, K., Holz, D. E., Bulik, T., & O'Shaughnessy, R. 2016, Natur, 534, 512
Biscoveanu, S., Callister, T. A., Haster, C.-J., et al. 2022, ApJ, 932, L19
Broekgaarden, F. S., Berger, E., Neijssel, C. J., et al. 2021, MNRAS, 508, 5028
Bruel, T., Lamberts, A., Rodriguez, C. L., et al. 2025, A&A, 701, A252
Callister, T. A. 2024, arXiv:2410.19145
Chernoff, D. F., & Finn, L. S. 1993, ApJ, 411, L5
Choksi, N., Gnedin, O. Y., & Li, H. 2018, MNRAS, 480, 2343
de, L. M., Rocha, L. S., Bernardo, A., Bachega, R. R. A., & Horvath, J. E. 2024, MNRAS, 535, 2041
Delaunay, B. 1934, Bulletin de l'Académie des Sciences de l'URSS. Classe des sciences mathématiques et naturelles, 6, 793
Di Carlo, U. N., Giacobbo, N., Mapelli, M., et al. 2019, MNRAS, 487, 2947
Dominik, M., Belczynski, K., Fryer, C., et al. 2012, ApJ, 759, 52
El-Badry, K., Quataert, E., Weisz, D. R., Choksi, N., & Boylan-Kolchin, M. 2019, MNRAS, 482, 4528
Eldridge, J. J., & Stanway, E. R. 2016, MNRAS, 462, 3302
Essick, R., & Fishbach, M. 2024, ApJ, 962, 169
Essick, R., Coughlin, M. W., Zevin, M., et al. 2025, PhRvD, 110, 102001
Farag, E., Renzo, M., Farmer, R., Chidester, M. T., & Timmes, F. X. 2022, ApJ, 937, 112
Farmer, R., Renzo, M., de Mink, S. E., Marchant, P., & Justham, S. 2019, ApJ, 887, 53
Farr, W. M., Fishbach, M., Ye, J., & Holz, D. 2019, ApJL, 883, L42
Fragos, T., Andrews, J. J., Bavera, S. S., et al. 2023, ApJS, 264, 45
Gennari, V., Mastrogiovanni, S., Tamanini, N., Marsat, S., & Pierra, G. 2025, PhRvD, 111, 123046
Gerosa, D., & Fishbach, M. 2021, NatAs, 5, 749
Guttman, N., Payne, E., Lasky, P. D., & Thrane, E. 2025, arXiv:2509.09876
Harris, C. R., Millman, K. J., van der Walt, S. J., et al. 2020, Natur, 585, 357
Heinzel, J., Mould, M., & Álvarez-López, S. 2025a, PhRvD, 111, 063043
Heinzel, J., Mould, M., & Vitale, S. 2025b, PhRvD, 111, L061305
Hendriks, D. D., van Son, L. A. C., Renzo, M., Izzard, R. G., & Farmer, R. 2023, MNRAS, 526, 4130
Karnesis, N., Katz, M. L., Korsakova, N., Gair, J. R., & Stergioulas, N. 2023, MNRAS, 526, 4814
Kullback, S., & Leibler, R. A. 1951, AnnMS, 22, 79
Lalleman, M., Turbang, K., Callister, T., & van Remortel, N. 2025, A&A, 698, A85
Lamberts, A., Garrison-Kimmel, S., Clausen, D. R., & Hopkins, P. F. 2016, MNRAS, 463, L31
LIGO Scientific Collaboration, Virgo Collaboration, & KAGRA Collaboration, et al. 2025a, arXiv:2509.04348
LIGO Scientific Collaboration, Virgo Collaboration, & KAGRA Collaboration, et al. 2025b, arXiv:2508.18083
LIGO Scientific Collaboration, Virgo Collaboration, & KAGRA Collaboration, et al. 2025c, arXiv:2508.18082
Mancarella, M., & Gerosa, D. 2025, PhRvD, 111, 103012
Mandel, I., & Farmer, A. 2022, PhR, 955, 1
Mandel, I., Farr, W. M., & Gair, J. R. 2019, MNRAS, 486, 1086
Mapelli, M. 2021, Handbook of Gravitational Wave Astronomy (Springer)
Mapelli, M., Bouffanais, Y., Santoliquido, F., Sedda, M. A., & Artale, M. C. 2022, MNRAS, 511, 5797
Mapelli, M., Giacobbo, N., Ripamonti, E., & Spera, M. 2017, MNRAS, 472, 2422
Mapelli, M., Giacobbo, N., Santoliquido, F., & Artale, M. C. 2019, MNRAS, 487, 2
Markovic, D. 1993, PhRvD, 48, 4738
Mastrogiovanni, S., Leyde, K., Karathanasis, C., et al. 2021, PhRvD, 104, 062009
Mukherjee, S. 2022, MNRAS, 515, 5495
Neijssel, C. J., Vigna-Gómez, A., Stevenson, S., et al. 2019, MNRAS, 490, 3740
Payne, E., & Thrane, E. 2023, PhRvR, 5, 023013
Rajan, V. T. 1994, Discrete Comput. Geom., 12, 189
Ray, A., Magaña Hernandez, I., Mohite, S., Creighton, J., & Kapadia, S. 2023, ApJ, 957, 37
Rinaldi, S., Del Pozzo, W., Mapelli, M., Lorenzo-Medina, A., & Dent, T. 2024, A&A, 684, A204
Rinaldi, S., Liang, Y., Demasi, G., Mapelli, M., & Del Pozzo, W. 2025, A&A, 702, A52
Rippa, S. 1990, Comput. Aided Geom. Des., 7, 489
Robitaille, T. P., et al. 2013, A&A, 558, A33
Rodriguez, C. L., Chatterjee, S., & Rasio, F. A. 2016, PhRvD, 93, 084029
Rodriguez, C. L., & Loeb, A. 2018, ApJL, 866, L5
Sadiq, J., Dent, T., & Lorenzo-Medina, A. 2025, PhRvD, 112, 083028
Sadiq, J., Dent, T., & Wysocki, D. 2022, PhRvD, 105, 123014
Santini, A., Gerosa, D., Cotesta, R., & Berti, E. 2023, PhRvD, 108, 083033
Schneider, F. R. N., Podsiadlowski, P., & Laplace, E. 2023, ApJL, 950, L9
Schneider, F. R. N., Podsiadlowski, P., & Müller, B. 2021, A&A, 645, A5
Sedda, M. A., Kamlah, A. W. H., Spurzem, R., et al. 2024, MNRAS, 528, 5140
Sedda, M. A., Mapelli, M., Benacquista, M., & Spera, M. 2023, MNRAS, 520, 5259
Stevenson, S., Sampson, M., Powell, J., et al. 2019, ApJ, 882, 121
Tagawa, H., Haiman, Z., & Kocsis, B. 2020, ApJ, 898, 25
Talbot, C., & Golomb, J. 2023, MNRAS, 526, 3495
Talbot, C., & Thrane, E. 2018, ApJ, 856, 173
Tong, H., Fishbach, M., Thrane, E., et al. 2025, arXiv:2509.04151
Torniamenti, S., Mapelli, M., Périgois, C., et al. 2024, A&A, 688, A148
Toubiana, A., Katz, M. L., & Gair, J. R. 2023, MNRAS, 524, 5844
Toubiana, A., Gerosa, D., Mould, M., et al. 2025, arXiv:2507.13249
van Son, L. A. C., de Mink, S. E., Callister, T., et al. 2022, ApJ, 931, 17
Virtanen, P., Gommers, R., & Oliphant, T. E. 2020, NatMe, 17, 261
Vitale, S., Gerosa, D., Farr, W. M., & Taylor, S. R. 2020, Handbook of Gravitational Wave Astronomy (Springer)
Woosley, S. E. 2017, ApJ, 836, 244
Yang, Y., et al. 2019, PhRvL, 123, 181101
Ye, C. S., & Fishbach, M. 2024, ApJ, 967, 62
Ye, C. S., Fishbach, M., Kremer, K., & Reina-Campos, M. 2025, arXiv:2507.07183
Zevin, M., Bavera, S. S., Berry, C. P. L., et al. 2021, ApJ, 910, 152